Supplementary Information

Shining a light on methane dry reforming – exploring the impact of visible light on carbon formation over $Co/xCeO_2$-Al_2O_3

George E. P. O'Connell[1], Richard F. Webster[2], Elise Elkington[1], Rose Amal[1], Jason Scott[1*], Emma C. Lovell[1*]

[1] Particles and Catalysis Research Group, School of Chemical Engineering, The University of New South Wales, Sydney, NSW 2052, Australia

[2] Electron Microscopy Unit, The University of New South Wales, Sydney, NSW, 2052, Australia

* Corresponding authors: e.lovell@unsw.edu.au, jason.scott@unsw.edu.au

Table of Contents

S1 Experimental Calculations

Equation S1 determined the molar ratio between Al and Ce for the flame spray synthesis. The CO_2 conversion, CH_4 conversion, the H_2/CO generation rates and the H_2/CO ratio were the metrics employed to assess the performance (Equations S2, S3, S4 and S5, respectively). The light enhancement was calculated on a thermal basis (Equation S6). Equation S7 was used to calculate the CO_2 and CH_4 conversion deactivation extent, which was defined as the activity lost compared to the initial value.

$$xCe\text{-}Al, x = \frac{n_{Al}}{n_{Al} + n_{Ce}} \times 100 \ \#(S1)$$

$$CO_2\ Conversion, X_{CO_2}\ (\%) = \frac{\dot{F}_{CO_2,in} - \dot{F}_{CO_2,out}}{\dot{F}_{CO_2,in}} \times 100\% \ \#(S2)$$

$$CH_4\ Conversion, X_{CH_4}\ (\%) = \frac{\dot{F}_{CH_4,in} - \dot{F}_{CH_4,out}}{\dot{F}_{CH_4,in}} \times 100\% \#(S3)$$

$$x\ Produced\ \left(\dot{n}_x, mmol g_{cat}^{-1} h^{-1}, x = H_2\ or\ CO\right) = \frac{\dot{F}_{X,out}}{m_{cat} \times V_m^0}\ ,\ V_m^0 = 22.4 mL mmol^{-1}, \#(S4)$$

$$H_2/CO\ Ratio = \frac{\dot{n}_{H_2}}{\dot{n}_{CO}} \#(S5)$$

$$Light\ Enhancement\ of\ x, x = CO_2\ or\ CH_4\ (\%) = \frac{X_{x,VL} - X_{x,Th}}{X_{x,Th}} \times 100\% \ \#(S6)$$

$$Deactivation\ Extent\ of\ x, x = CO_2\ or\ CH_4\ (\%) = \frac{X_{x,\ initial} - X_{x,final}}{X_{x,initial}} \times 100\% \ \#(S7)$$

The fractional cobalt loading was determined from ICP-OES (Equation S8). The Scherrer equation (Equation S9) was used to find the crystallite size of Al_2O_3, CeO_2 and Co_3O_4 from XRD.

$$Fractional\ Co\ Loading\ (\%) = \frac{Co\ (wt\%)}{Co\ (wt\%) + Al\ (wt\%) + Ce\ (wt\%)} \times 100\% \ \#(S8)$$

$$\tau = \frac{K\lambda}{\beta cos\theta} \ \#(S9)$$

The theoretical H_2 consumption was calculated assuming no support was reduced, as the extent of support reduction cannot be accounted for. The actual Co loading determined by ICP-OES was employed for these calculations. A two-step cobalt reduction pathway was assumed, as outlined by Liu et al. (Equations S10 and S11) [1]. With these assumptions, the quantity of hydrogen consumed was calculated via Equation S12.

$$Co_3O_4 + H_2 \rightarrow 3CoO + H_2O \ \#(S10)$$

$$3CoO + 3H_2 \rightarrow 3Co + 3H_2O \ \#(S11)$$

$$n_{H_2} = \left(\frac{4}{3}\right) \times \frac{\frac{m_{cat} \times x_{Co}}{M_{r,\ Co}}}{m_{cat}} \#(S12)$$

The XPS Al/Ce ratio was calculated using Equations S13 – S15, and the amount of Ce^{3+} relative to Ce^{3+} was calculated using Equation S16.

$$n_{Al}\,(mol\%) = 100\% \times \frac{a_{Al} \times M_{r,\,Al}}{\sum(a_i \times M_{r,i})} \#(S13)$$

$$n_{Ce}\,(mol\%) = 100\% \times \frac{a_{Ce} \times M_{r,\,Ce}}{\sum(a_i \times M_{r,i})} \#(S14)$$

$$Al/Ce = \frac{n_{Al}}{n_{Ce}} \#(S15)$$

$$Amount\ Ce^{3+} = 100\% \times \frac{Ce^{3+}}{Ce^{3+} + Ce^{4+}} \#(S16)$$

1

S2 Further Experimental Details

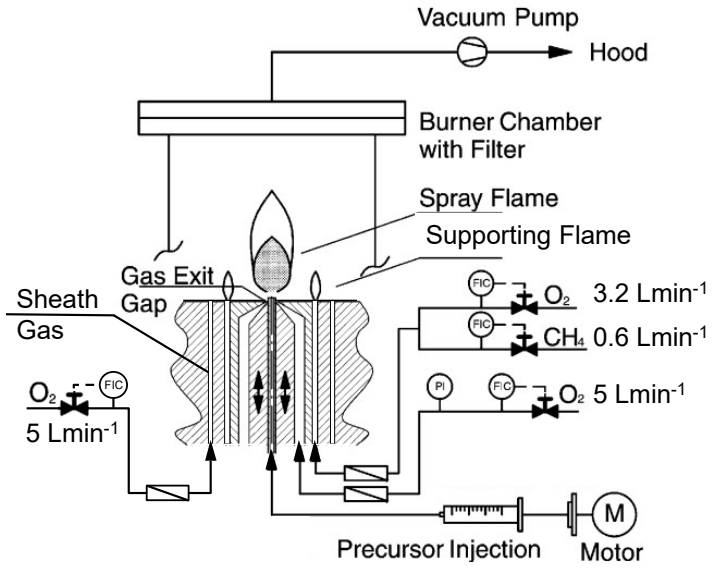

Figure S1: FSP experimental set up. Image adapted from Madler et al. [2] to include sheath line and gas flowrates used in this work.

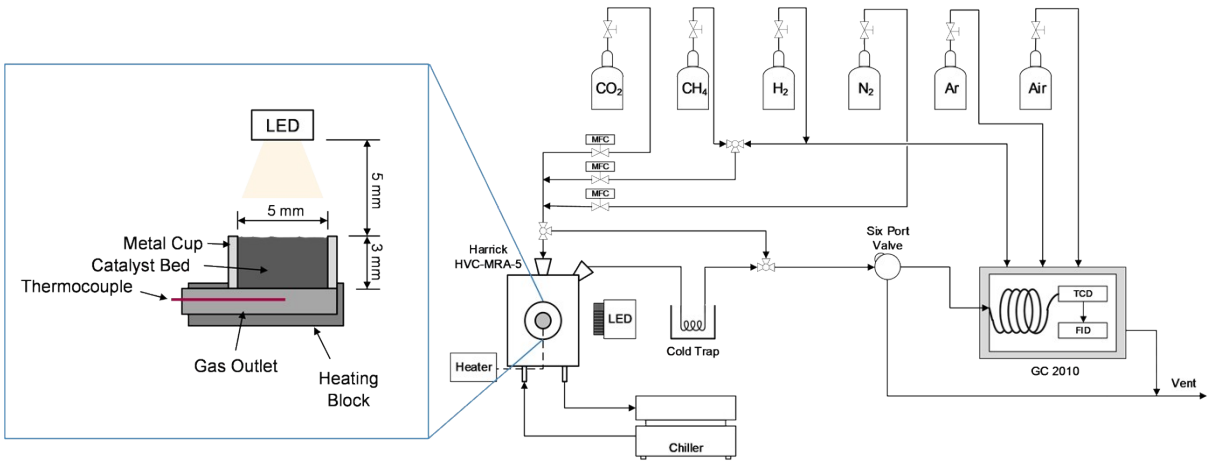

Figure S2: Schematic detailing the in-house reactor setup using a Harrick high-temperature Raman cell and a Shimadzu GC 2010 to measure the effluent gas composition. The blue inset details the sample cup identifying the thermocouple location, and LED mounted 5 mm above a 5 mm diameter aperture for visible light-illumination.

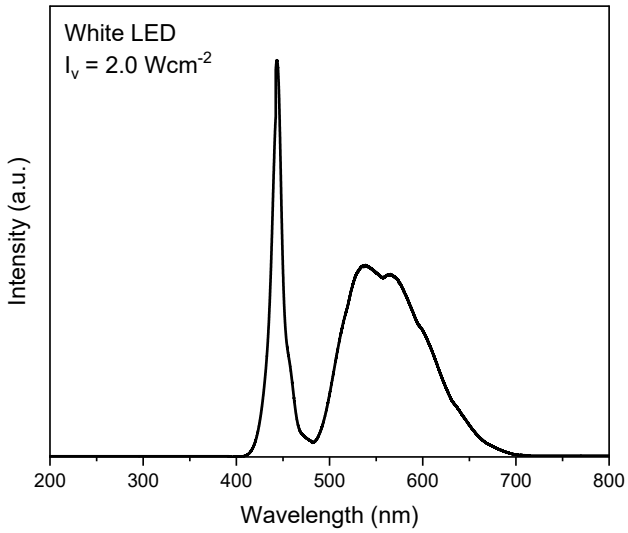

Figure S3: White LED emission spectra. The spectra was obtained from Optical Emission Spectroscopy (OES) using a Princeton Instruments SpectraPro HRS-500 spectrograph with a blaze wavelength of 500 nm and grating of 1200 linesmm^{-1}.

S3 Activity Results

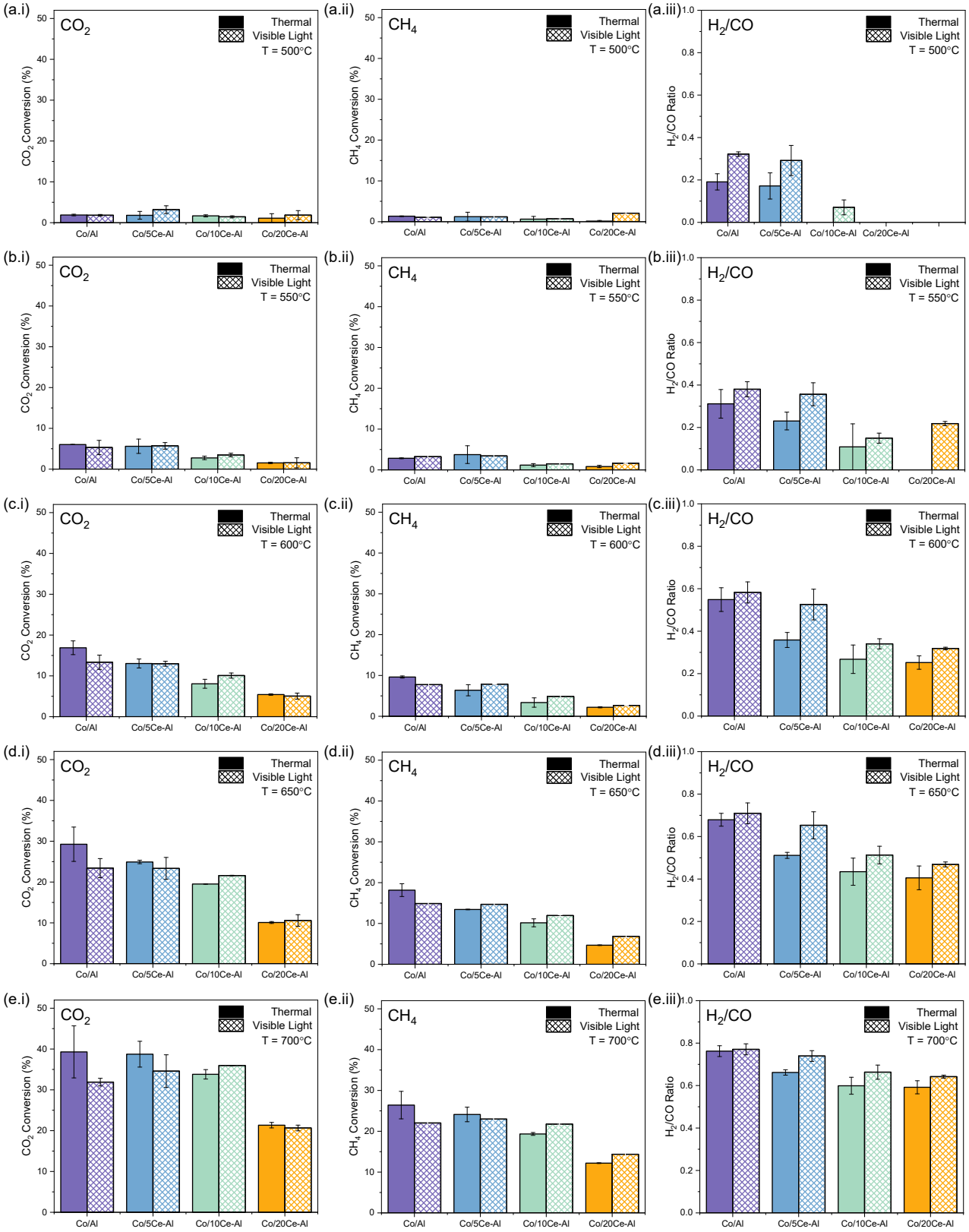

Figure S4: Incremental temperature tests of the Co/xCe-Al catalysts under thermal (■) and visible light-assisted (▒) reaction conditions at (a) 500 °C, (b) 550 °C, (c) 600 °C, (d) 650 °C and (e) 700 °C showing (i) CO_2 conversion, (ii) CH_4 Conversion and (iii) H_2/CO ratio. Catalysts were reduced and passivated ex-situ *at 850 °C for 1 h, then* in-situ *at 550 °C for 1h (GHSV = 12 000 h^{-1}, CO_2/CH_4 = 1).*

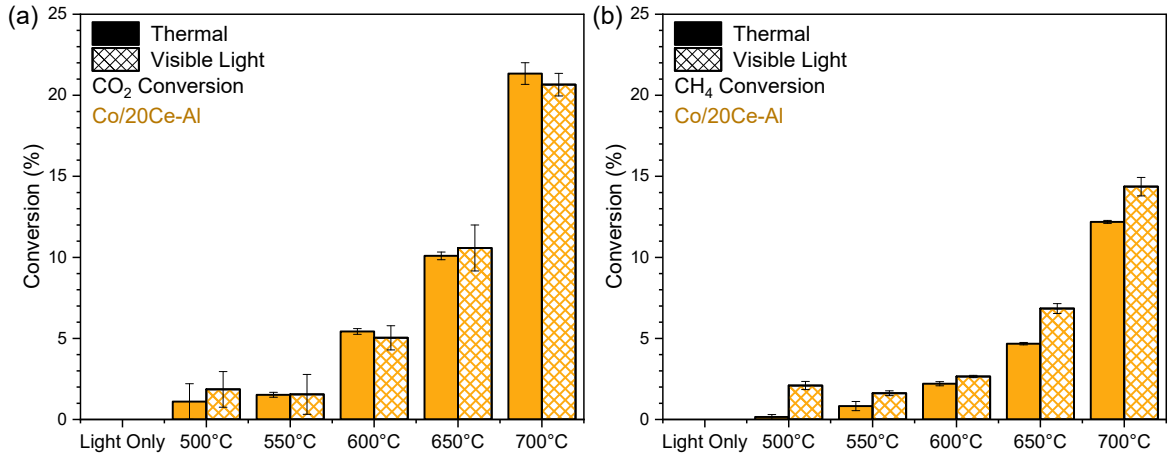

Figure S5: (a) CO_2 conversion and (b) CH_4 conversion of the Co/20Ce-Al catalyst under thermal catalysts under thermal (■) and visible light-assisted (▒) reaction conditions at various temperatures. The "light only" experiment was conducted with no thermal energy input. Catalysts were reduced and passivated ex-situ *at 850 °C for 1 h, then* in-situ *at 550 °C for 1h (GHSV = 12 000 h^{-1}, CO_2/CH_4 = 1).*

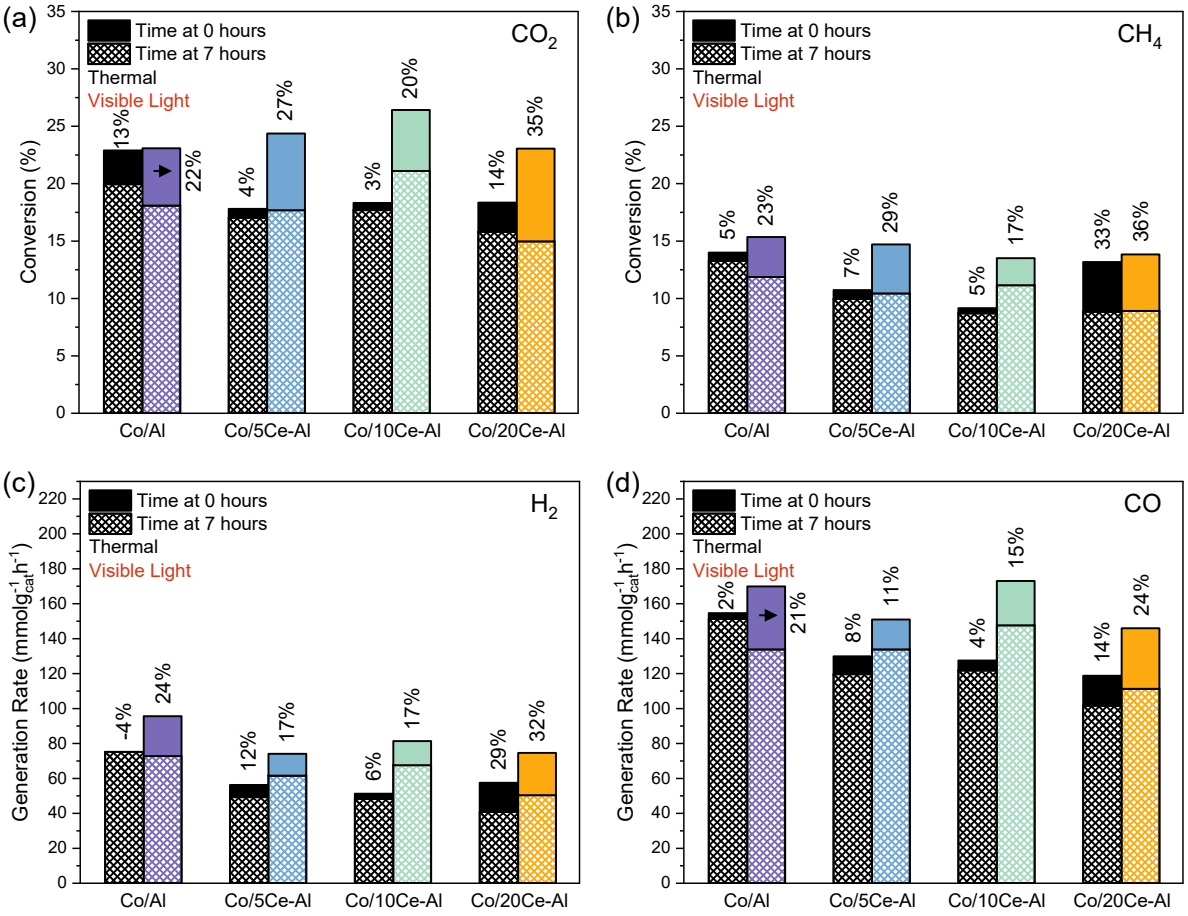

Figure S6: (a) CO_2 conversion, (b) CH_4 conversion, (c) H_2 generation rate and (d) CO generation rate of the Co/xCe-Al stability tests. All catalysts were reduced and passivated ex-situ *for 1 h at 850 °C and then* in-situ *at 550 °C for 1 h. The reaction was run under thermal (black) and visible light-assisted (coloured) reaction conditions. The initial conversion/product generation is represented as ■ and the conversion after 7 h is shown as ▒. The percentages refer to the difference in activity between 0 h and 7 h. (T = 650 °C, GHSV = 12 000 h^{-1}, CO_2/CH_4 = 1)*

S4 Thermal Gravimetric Analysis and Raman Spectroscopy

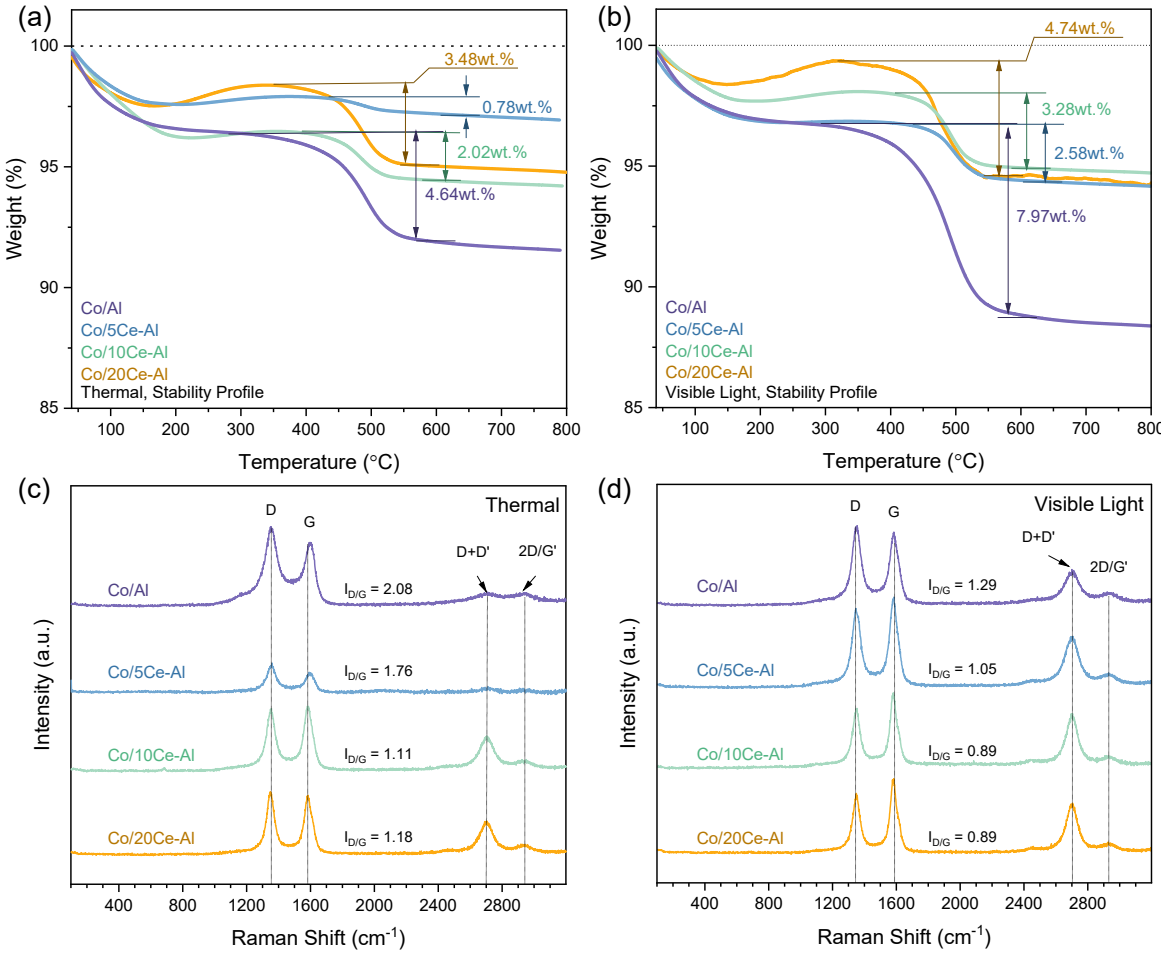

Figure S7: TGA curves of the spent Co/xCe-Al catalysts (from 7 h stability test at 650 °C) under (a) thermal and (b) visible light-assisted reaction conditions. Raman spectroscopy of the spent stability tests under (c) thermal and (d) visible light reaction conditions. The $I_{D/G}$ ratio was calculated by integrating the prominent D and G bands.

S5 N_2 Physisorption Isotherms

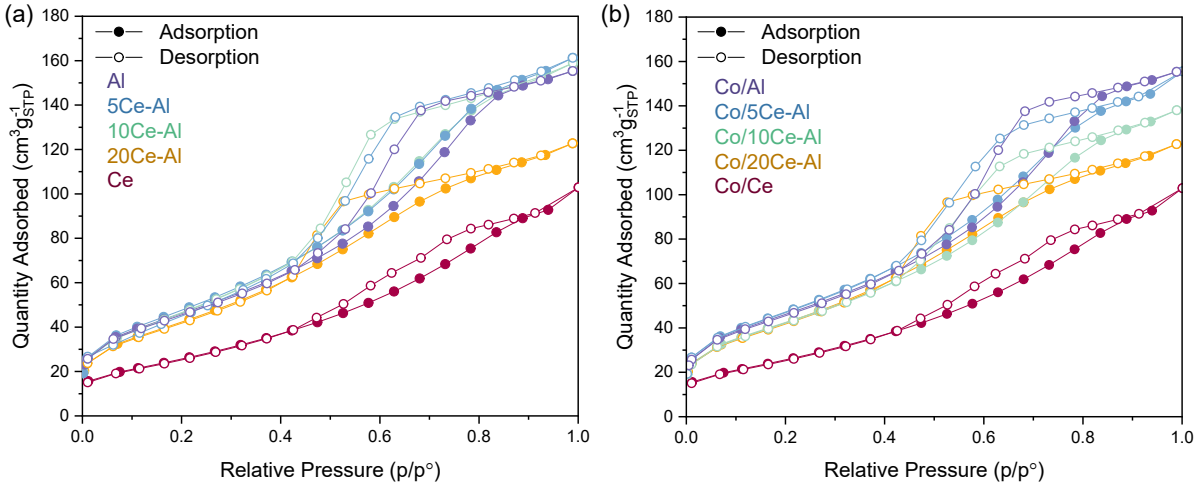

Figure S8: N_2 physisorption isotherms for (a) xCe-Al supports and (b) Co/xCe-Al catalysts.

S6 X-Ray Diffraction – Ceria's (111) and Alumina's (440) Phases

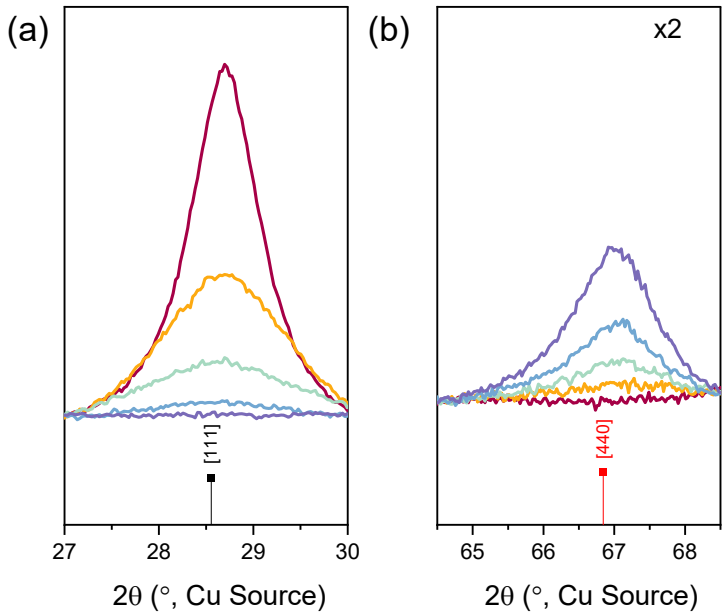

Figure S9: Overlaid X-ray diffraction patterns of the Al (purple), 5Ce-Al (blue), 10Ce-Al (green), 20Ce-Al (yellow) and Ce (red) supports for (a) ceria's (111) phase and (b) alumina's (440) phase, which was magnified to twice the initial size. This figure demonstrates the gradual decrease in the peak intensity as the concentration of Ce and Al decreases.

Table S1: XRD ceria's (111) phase and alumina's (440) phase 2θ peak positions.

Support	CeO_2 Position (2θ, °)	Al_2O_3 Position (2θ, °)
Al	n.d.	66.9
5Ce-Al	28.6	66.9
10Ce-Al	28.6	67.0
20Ce-Al	28.7	67.3
Ce	28.7	n.d.

S7 Quantitative X-Ray Diffraction (Rietveld Refinement)

The phase quantification and experimental lattice parameters of CeO_2 and γ-Al_2O_3 were determined through Rietveld refinement. Crystallographic data was obtained from the CeO_2 and Al_2O_3 cards matched using X'Pert HighScore software (ICSD ref#002-8260 for CeO_2 and ICSD ref#062-1707 for γ-Al_2O_3. The refinement was iterated until an excellent fit was obtained (R_{exp} < 3, goodness of fit (GOF or χ^2) < 5 and $R_B \approx 10$) (Table S2) [3]. The CeO_2 data fit closely to the matched phase, as did the major crystalline peaks of γ-Al_2O_3, although there was consistent discrepancy for the peaks from 35° to 45 ° for the 10Ce-Al, 5Ce-Al, and Al supports (Figure S10). Fitting the pure alumina sample to other alumina phases (η, θ), the inclusion of aluminium hydroxide, and multiphase analysis (combined γ and η/θ) only reduced the accuracy of the refinement, availing no solution. For 10Ce-Al and 5Ce-Al, the small discrepancy could be attributed to $CeAlO_3$ (100% intensity peak (110) at 33.7°, ICSD ref#007-2558), however, the peaks overlap significantly, making quantitative analysis difficult. As the error was pronounced for the neat Al_2O_3 support, it was unlikely that $CeAlO_3$ caused this error. The lattice parameters were found by refining the unit cell, but meaningful understanding is limited, particularly for 5Ce-Al, 10Ce-Al and 20Ce-Al due to the R_B >> 10 (Table S2).

Table S2: Expected profile R-value (R_{exp}), weighted profile R-value (R_{wp}), goodness of fit (GOF) and Bragg R-value fit indicators for Rietveld refinement. Experimental γ-Al_2O_3 and CeO_2 lattice parameters.

Support	R_{exp}	R_{wp}	GOF	R_B		Lattice Parameter	
				γ-Al_2O_3	CeO_2	γ-Al_2O_3	CeO_2
Al	3.066	6.106	3.967	11.0	n.d.	7.8794	n.d.
5Ce-Al	2.510	3.498	1.911	14.8	10.9	7.8810	5.3567
10Ce-Al	2.373	4.503	3.602	15.7	13.8	7.8886	5.4009
20Ce-Al	2.348	3.503	2.226	20.9	7.2	7.8723	5.4073
Ce	2.244	2.538	1.279	n.d.	2.7	n.d.	5.4072

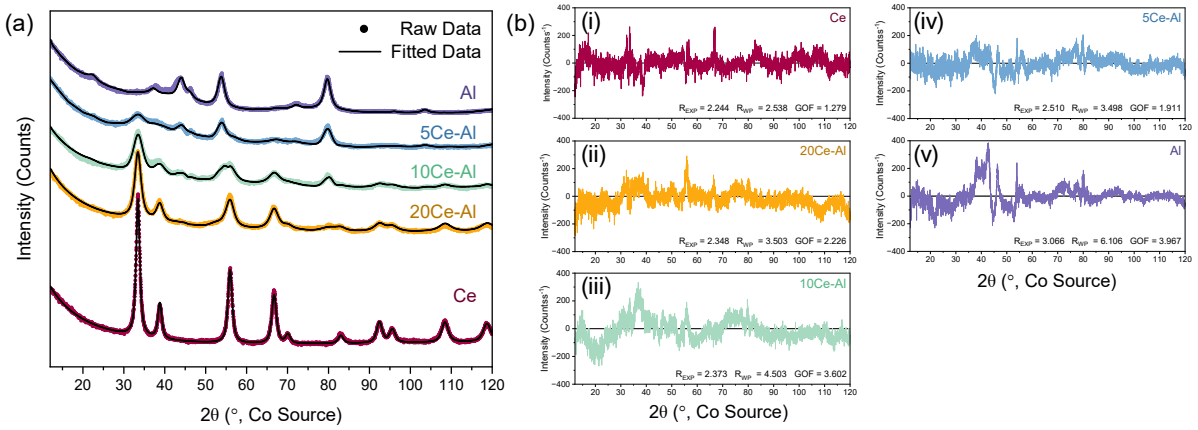

Figure S10: Rietveld refinement of the xCe-Al supports. (a) The overall fitted data to the xCe-Al patterns, (b) the difference plots for (i) Ce, (ii) 20Ce-Al, (iii) 10Ce-Al, (iv) 5Ce-Al and (v) Al.

S8 Raman Spectroscopy

Raman spectroscopy was employed to verify the change in SOV concentration with Ce incorporation and probe the vibrational modes of the xCe-Al supports. Ceria exhibited one peak at 464 cm^{-1}, corresponding to the F_{2g} vibrational mode (Figure S11) [4–6]. Conversely, γ-Al_2O_3 was Raman inactive [7]. As γ-Al_2O_3 became the dominant phase, the intensity of ceria's F_{2g} peak diminished (relative to neat CeO_2), as CeO_2 formed a lower proportion of the scattering volume [8]. The F_{2g} peak did not shift significantly for 20Ce-Al and 10Ce-Al, indicating no internal lattice strain for the ceria crystallites, confirming the XRD results. The insets in Figure S11 detail two CeO_2 SOV peaks corresponding to the SOV D-band at 580 – 600 cm^{-1} and to the superoxide species (O_2^-) at 1100 cm^{-1}, conducive to an O_2 species adsorbed onto a single electron surface oxygen vacancy [4,5].

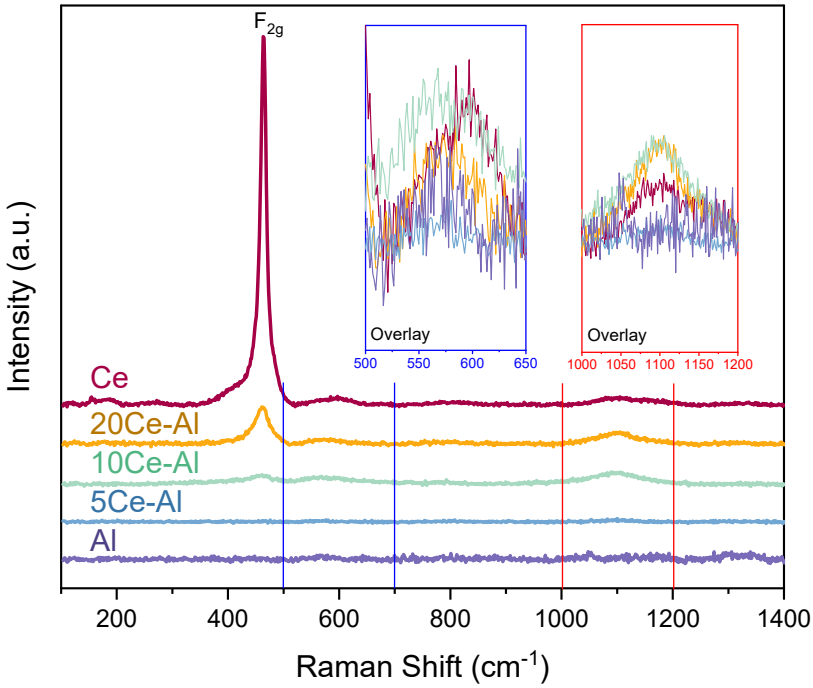

Figure S11: Raman spectroscopy of the xCe-Al supports. The insets depict two SOV peaks corresponding to the D-band vibrational mode from 500 – 650 cm^{-1} and a superoxide species (oxygen adsorbed to single electron vacancy) at 1000 – 1200 cm^{-1}.

S9 Identification of the Al_2O_3 α_4 H_2-TPR Peak

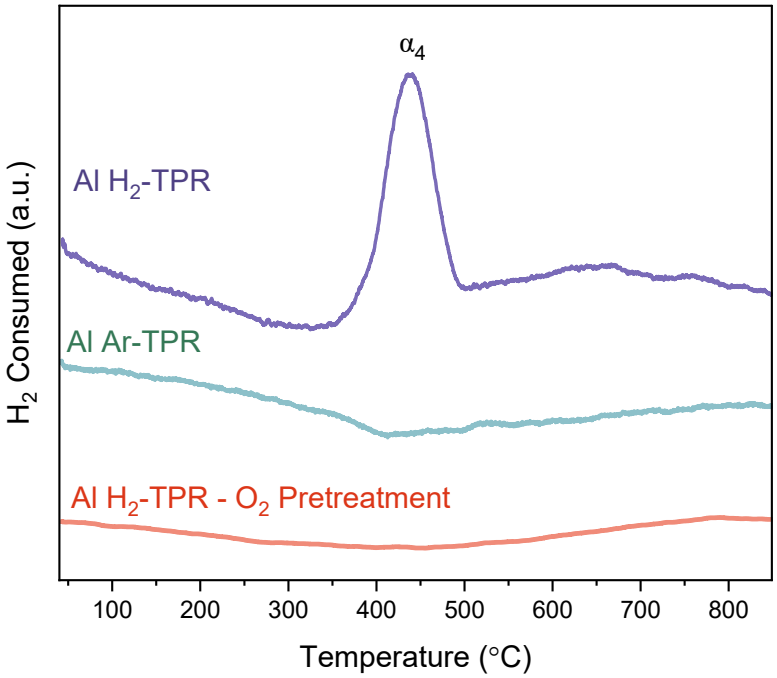

Figure S12: (a) H_2-TPR of the Al_2O_3 support (purple) shows the α_4 peak at 440 °C. The Ar-TPR of the Al_2O_3 support (red) indicated that the peak was not caused by the thermal decomposition of species. After pre-treating the Al_2O_3 support in O_2 (450 °C for 1 h, ramp rate of 10 °Cmin^{-1}), α_4 disappears, indicating that the species was most likely residue from the FSP synthesis process [9–11].

S10 X-Ray Diffraction of Co/xCe-Al

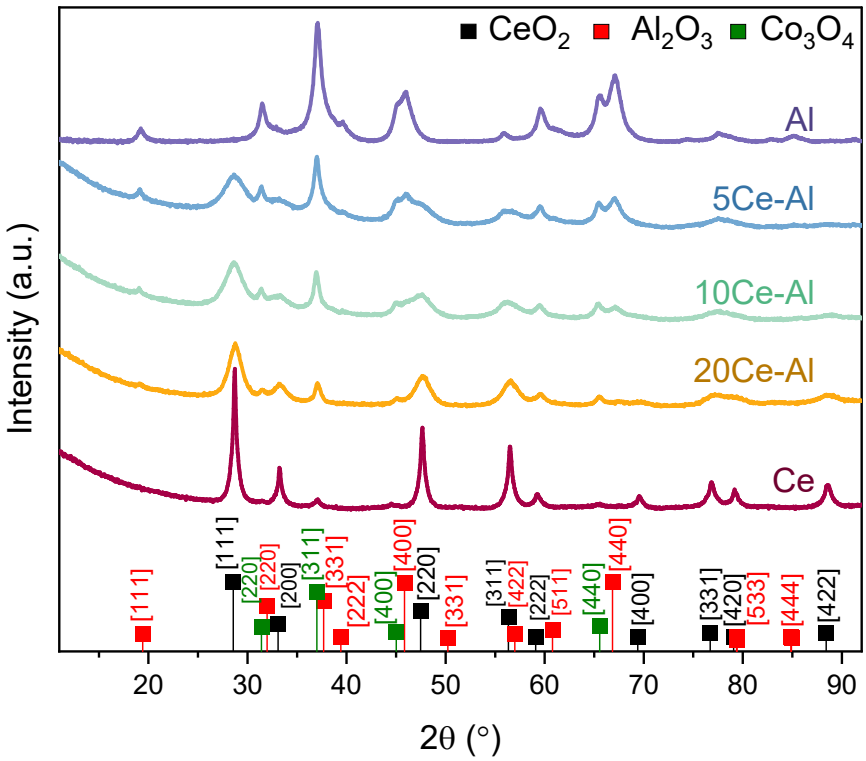

Figure S13: XRD profile of the as-prepared Co/xCe-Al catalysts, identifying the CeO_2 (black ICSD ref#062-1707), Al_2O_3 (red, ICSD ref#062-1707) and Co_3O_4 (green, ICDD ref. #006-9374). The (440) phase of Co_3O_4 was used to calculate the crystallite size, as it exhibited less overlap than the prominent (311) phase.

Table S3: Cobalt-loaded XRD ceria's (111), alumina's (440) and cobalt's (440) phase 2θ peak positions.

Catalyst	CeO_2 Position (2θ, °)	Al_2O_3 Position (2θ, °)	Co_3O_4 Position (2θ, °)
Co/Al	n.d.	67.0	65.5
Co/5Ce-Al	28.6	67.0	65.4
Co/10Ce-Al	28.6	67.0	65.4
Co/20Ce-Al	28.7	67.5	65.5
Co/Ce	28.7	n.d.	65.4

S11 H_2 Temperature-Programmed Reduction

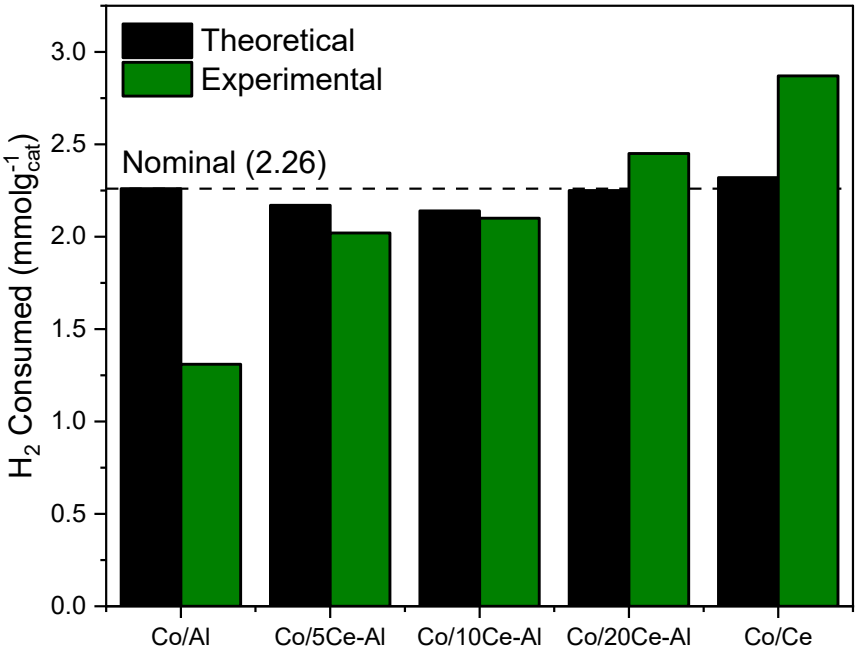

Figure S14: Comparison between the theoretical and the experimental hydrogen consumed. All calculations were performed using the actual Co loading, and the nominal H_2 consumed assumes a loading of 10.0 wt% Co.

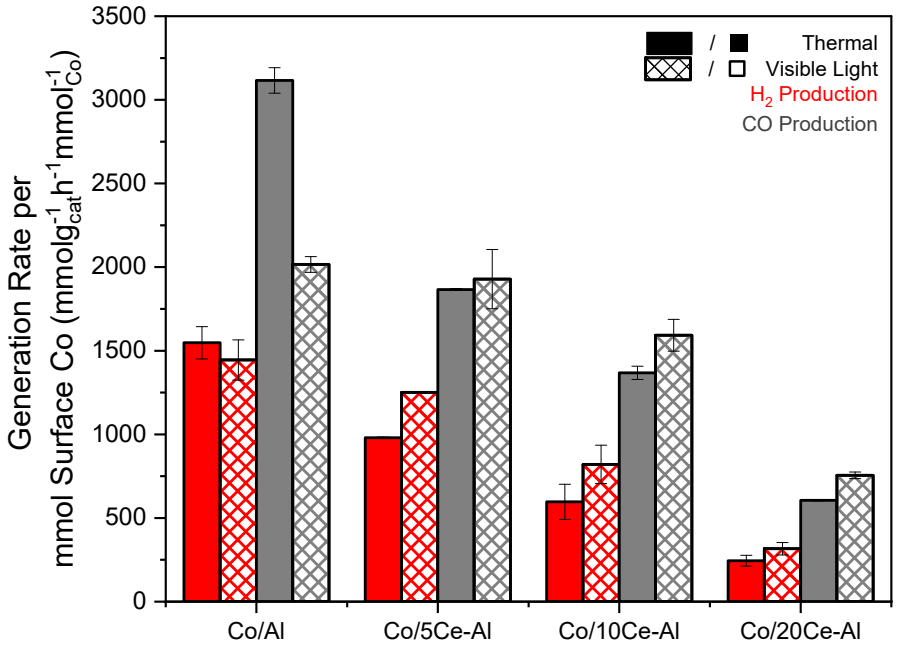

Figure S15: The H_2 (red) and CO (grey) production rates under thermal (■) and visible light-assisted (▒) reaction conditions when normalised to the amount of surface cobalt, as determined by XPS. The results highlight that the negative influence of Ce on the activity far outweighs the loss of Co from strong CoO anchoring to Al_2O_3.

S12 X-Ray Photoelectron Spectroscopy

Table S4: %Ce^{3+} (relative to Ce^{4+}) and ratio between Co^{3+} and Co^{2+} determined through XPS.

Catalyst	% Ce^{3+} (Relative to Ce^{4+})	Co^{3+}/Co^{2+} Ratio
Co/Al	n.d.	0.21
Co/5Ce-Al	41	0.33
Co/10Ce-Al	29	0.46
Co/20Ce-Al	29	0.67
Co/Ce	16	0.30

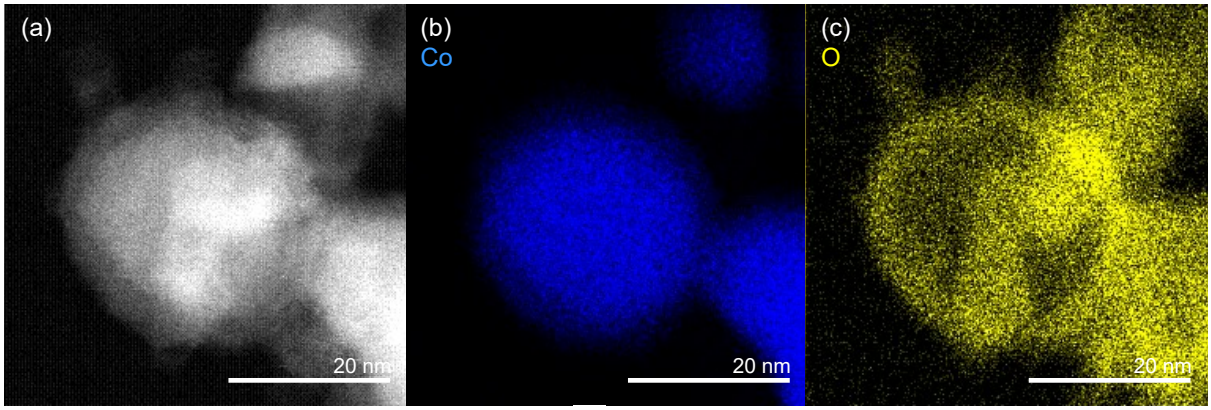

Figure S16: (a) 20 nm HAADF micrograph (b) Co EDS elemental map and (c) O EDS elemental map of a cobalt deposit (reduced and passivated Co/20Ce-Al catalyst), showing a cobalt oxide (likely Co_3O_4) passivation layer around a metallic cobalt core.

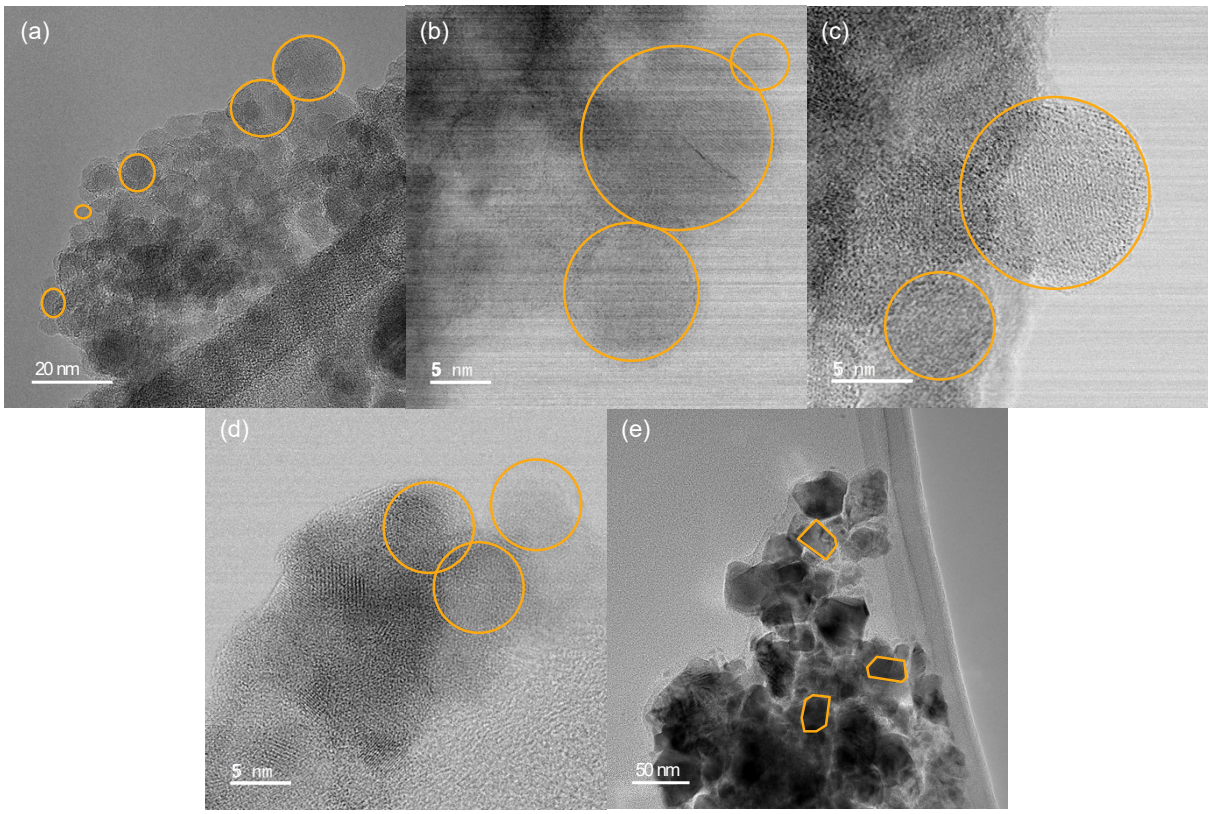

Figure S17: HR-TEM micrographs for the reduced and passivated (a) Co/Al, (b) Co/5Ce-Al, (c) Co/10Ce-Al, (d) Co/20Ce-Al and (e) Co/Ce control. The morphology of individual particles is outlined in yellow, demonstrating that all alumina samples contain spherical alumina crystals. The CeO_2 support, which is polyhedral in shape, is the only exception. The scale is represented on each micrograph.

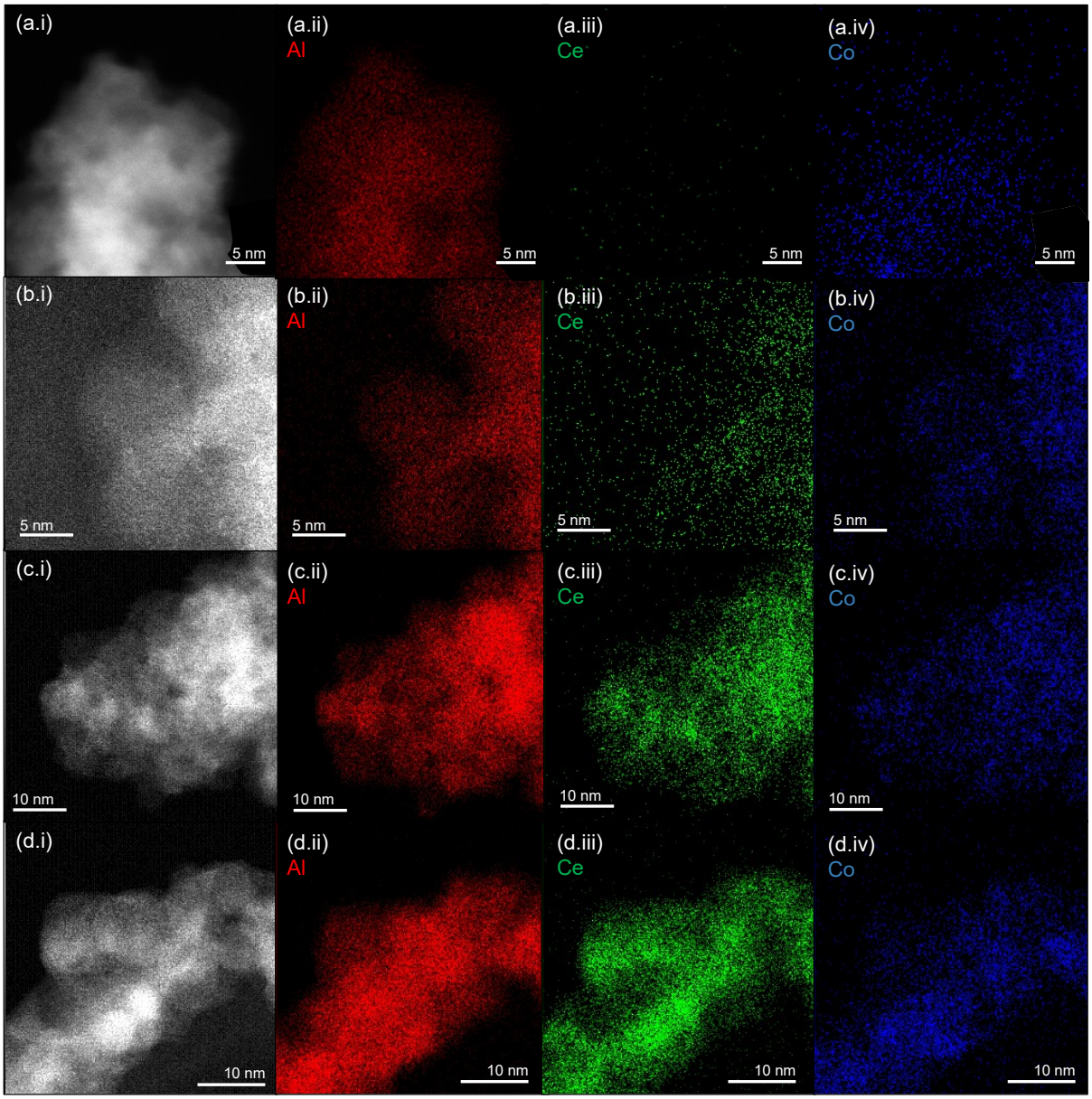

Figure S18: EDS mapping of the reduced and passivated (a) Co/Al, (b) Co/5Ce-Al, (c) Co/10Ce-Al and (d) Co/20Ce-Al, showing (i) the HAADF image, and the maps of (ii) Al, (iii) Ce and (iv) Co. The scale is represented on each image.

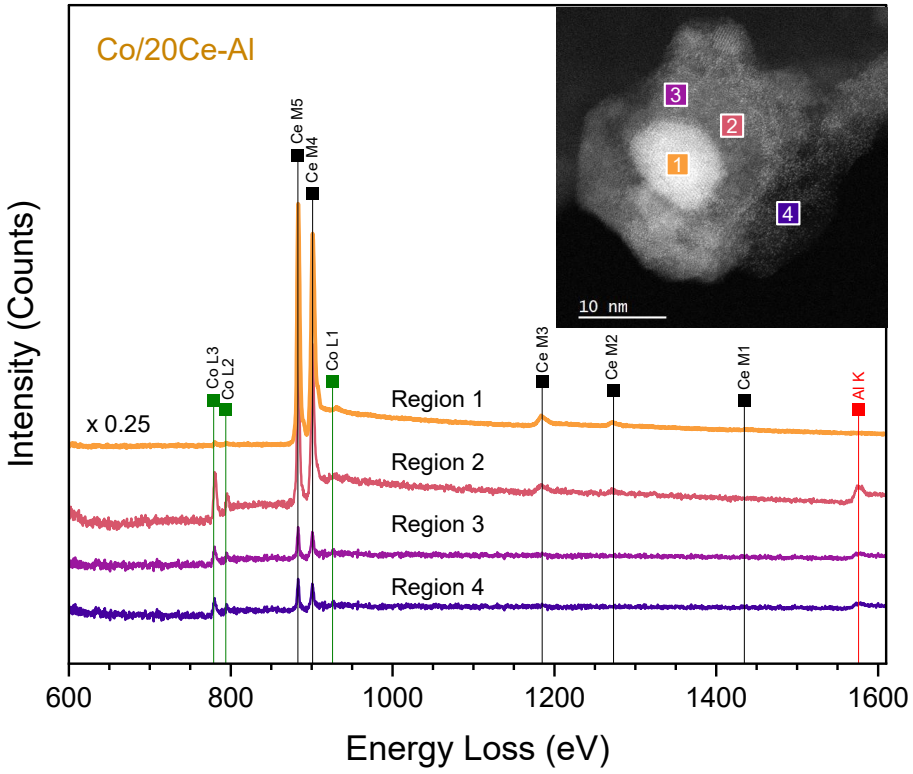

Figure S19: EELS spectra of the reduced and passivated Co/20Ce-Al catalyst. The EELS was recorded for four regions in close proximity, as identified by the HAADF inset.

S14 Transmission Electron Microscopy – Spent Catalysts

The Co deposit size was estimated by using the ImageJ software to measure the width of the carbon whiskers formed throughout the reaction. There was some variation in the whisker carbon diameter. In some instances, the width closely aligned with the diameter of the Co deposit (Figure S20a), but at other times, it was approximately 30% larger (Figure S20b and c), indicating the potential for overestimation of the Co deposit size. The size was measured from at least 400 different whiskers for each catalyst, and the distribution is provided in Figure S21.

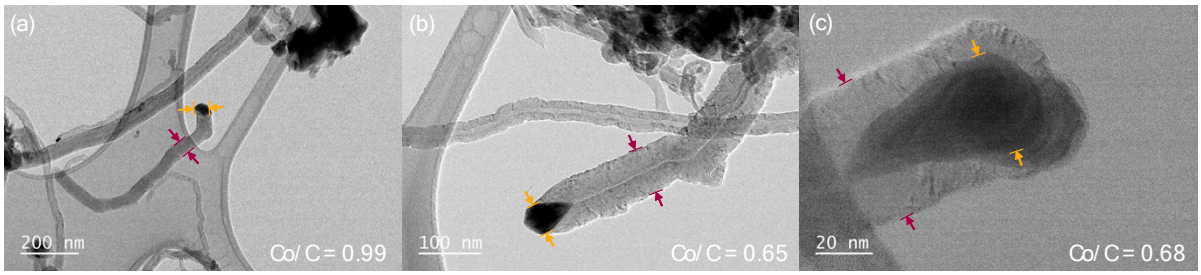

Figure S20: Comparison between the Co deposit ('Co') width and the carbon nanotube ('C') width of the spent catalysts. TEM images are of the spent Co/10Ce-Al ((a) and (b)) and Co/20Ce-Al (c) catalysts.

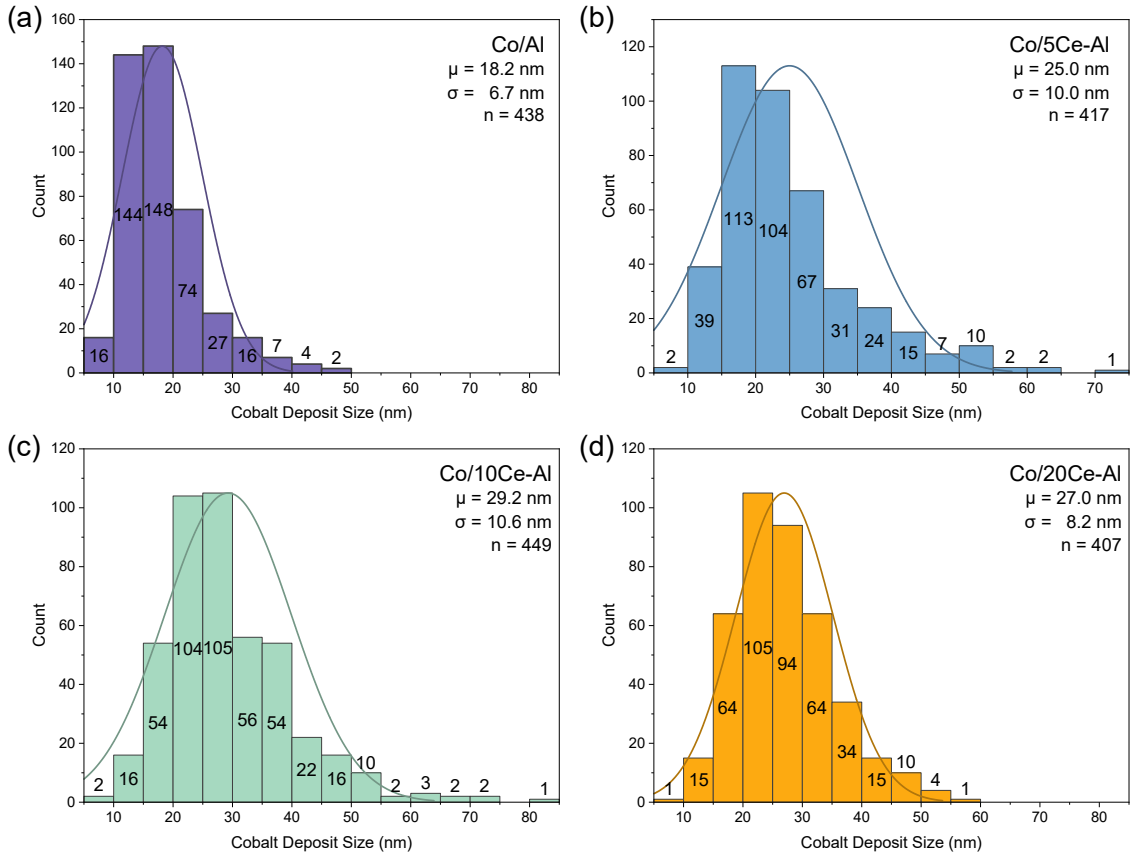

Figure S21: Co Size distribution of the spent (a) Co/Al, (b) Co/5Ce-Al, (c) Co/10Ce-Al and (d) Co/20Ce-Al catalysts.

S15 *In-Situ* Diffuse Reflectance Infrared Fourier Transform Spectroscopy

Table S5: In-situ *DRIFTS peak assignment for Al_2O_3 and CeO_2 supported catalysts in literature.*

Assigned Species	**Vibrational Mode: Wavenumber (cm^{-1})**			
	Al_2O_3 Support	**Ref.**	**CeO_2 Support**	**Ref.**
Gaseous Species				
CO	ν(CO): 2143	9,12	ν(CO): 2143	12
CO_2	ν(CO): 2200 – 2400	10	ν(CO): 2200 – 2400	13,14
CH_4	ν(CH): 3016 δ(CH): 1305	10	ν(CH): 3016 δ(CH): 1305	13,14
Surface Adsorbed Carbonyls (C ═ O) and Carbonates (CO_3) and CO				
Bidentate Carbonate [B]	ν_{as}(OCO): 1665 – 1690 ν_s(OCO): 1308 – 1350	9,11	ν_{as}(OCO): 1545 – 1580 ν_s(OCO): 1289 – 1300	13,14
Bridged Carbonate [Br]	ν_{as}(OCO): 1700 ν_s(OCO): 1300 – 1310	11	ν_{as}(OCO): 1736 ν_s(OCO): 1135	15,16
CO on Co^0 [CO_{ads}]	ν(CO): 1800 – 2080	9,10,12	ν(CO): 1940 – 2000	14,17
CH_xO (x = 1 – 3)	ν(CO): 1750	18,19	ν(CH): 2840 ν(CO): 1100	20
Hydrogen Carbonate (Bicarbonate) [H]	ν_{as}(OCO): 1627 – 1657 δ(COH):1435 – 1445 ν_s(OCO): 1225 – 1236	9–11	ν_{as}(OCO): 1599 – 1613 ν_s(OCO): 1391 – 1413 δ(COH): 1216 – 1218	13,14
Formate [F]	δ(CH): 2998 ν(CH): 2905 – 2907 δ(CH): 2768 ν_{as}(OCO): 1593 – 1597 δ(COH):1392 ν_s(OCO): 1372 – 1375	9,10	δ(CH): 2955 – 2974 ν (CH): 2845 – 2852 δ(CH): 2735 –2751 ν_{as}(OCO): 1547 – 1584 δ(COH): 1369 – 1373 ν_s(OCO): 1329 – 1360	13,14
Methoxy [MO]	ν(CH): 2841 ν(CO): 1097 – 1109	21	ν(CH): 2830 ν(CO): 1000 – 1100 ν(CO): 850	20,22,23
Monodendate Carbonate [M]	ν_{as}(OCO): 1510 – 1550 ν_s(OCO): 1370 – 1390	9,11	ν_{as}(OCO): 1504 ν_s(OCO): 1351	15,16
Polydentate Carbonate [P]	n.d.		ν_{as}(OCO): 1456 – 1490 ν(OCO): 1348 – 1380	14,17

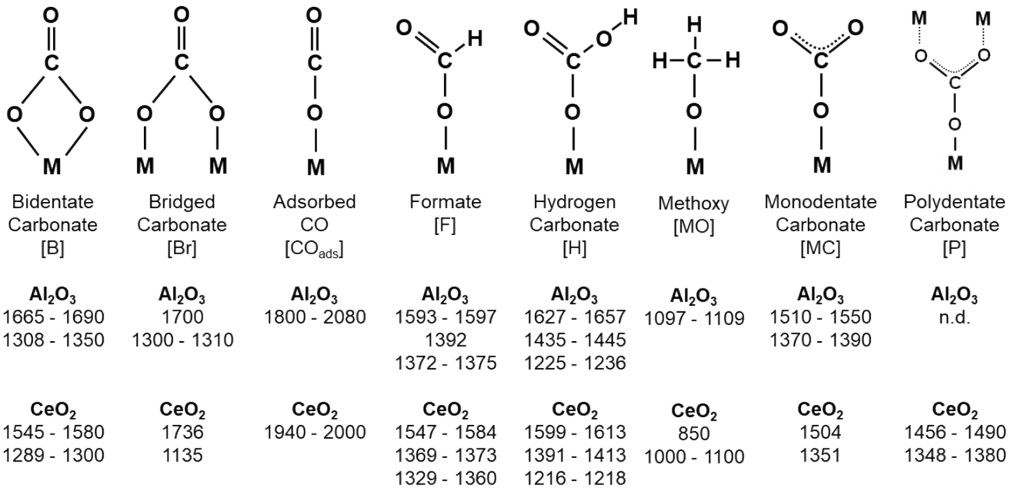

Figure S22: Molecular structure of adsorbed carbonyl and carbonate species with corresponding peak positions for Al_2O_3 and CeO_2. Image adapted from O'Connell et al. [14].

In-situ DRIFTS was performed on the Co/Al and Co/10Ce-Al catalysts to understand changes in the reaction mechanism with Ce incorporation and visible light illumination. Several sources were used to identify the vibrational modes of possible intermediates over Al_2O_3 and CeO_2 (Table S5, Figure S22). The catalyst was diluted with commercial γ-Al_2O_3 to prevent carbon build-up and clogging of the *in-situ* cell. The activity results identified a small concentration of H_2 and CO at 500 °C, so the DRIFTS spectra were obtained at 350, 450 and 550 °C, representing the surface adsorbed species before the reaction commenced, as the reaction began and after the reaction commenced.

Within the C–O fingerprint region (2200 – 1000 cm^{-1}, Figure S23a), singularly coordinated carbonyl species such as hydrogen carbonate (HCO_3^-, 'H' – ν_{as}(OCO) = 1650 cm^{-1}, δ(COH) = 1444 cm^{-1}), formate ('F' – ν_{as}(OCO) = 1591 cm^{-1}, δ(COH) = 1392 cm^{-1}, ν_s(OCO) = 1351 cm^{-1}) and monodentate carbonate ('M' – ν_{as}(OCO) = 1518 cm^{-1}, ν_s(OCO) = 1351 cm^{-1}) were evident. There was no evidence of the methoxy (ν(CH) ≈ 2840 cm^{-1}, ν(CO) ≈ 1100 cm^{-1}) or CH_xO (ν(CO) ≈ 1750 cm^{-1}) [18,19], indicating that the species may not be present for this catalytic system. Peak deconvolution of the C-O region was challenging, as many peaks overlapped. In the O–H/C–H region (3800 – 2500 cm^{-1}, Figure S23b), several peaks were evident (3732, 3700, 3627 and 3596 cm^{-1}) attributed to the stretching bands surface hydroxyl species of Al_2O_3 [11,12]. The C-H region was dominated by the stretching vibration of gaseous CH_4 (3015 cm^{-1}) and corresponding combination bands spanning 2800 – 3200 cm^{-1} [14]. The intensity of these combination bands obscured all ν(CH) vibrational modes of the other adsorbed species. The δ(COH) mode of CH_4 gas was evident in the C-O fingerprint region at 1305 cm^{-1}.

Before the reaction commenced (i.e. at 350 °C), the thermal Co/Al catalyst demonstrated strong HCO_3^-, formate and monodentate carbonate peaks (red line, Figure S23a). As the temperature increased to 450 °C, the intensity of the HCO_3^- and formate vibrational modes both diminished, indicating that both species are involved in the reaction mechanism. The asymmetrical stretching band of monodentate carbonate exhibited no change between 350 °C and 550 °C, indicating the species was either in dynamic equilibrium or inactive. After purging with Ar for 1 h at 550 °C, the monodentate carbonate remained, signifying that the species was unreactive at these temperatures (Figure S24). A single CO peak corresponding to CO adsorbed onto metallic Co was evident at ~ 1970 cm^{-1}, which decreased in intensity as the temperature increased, suggesting that removing CO_{ads} is not an energy-intensive reaction step. Interestingly, at 550 °C, two vibrational peaks appeared at 2110 and 2177 cm^{-1}. These peaks are assigned to the high oxidation state cations of Co^{2+} and Al^{3+} (exposed Al^{3+} coordinated octahedrally) [12]. Ji et al. suggested that these peaks represent CO_{ads} donating an electron to the Al^{3+} and Co^{2+} sites through a σ coordination bond [12].

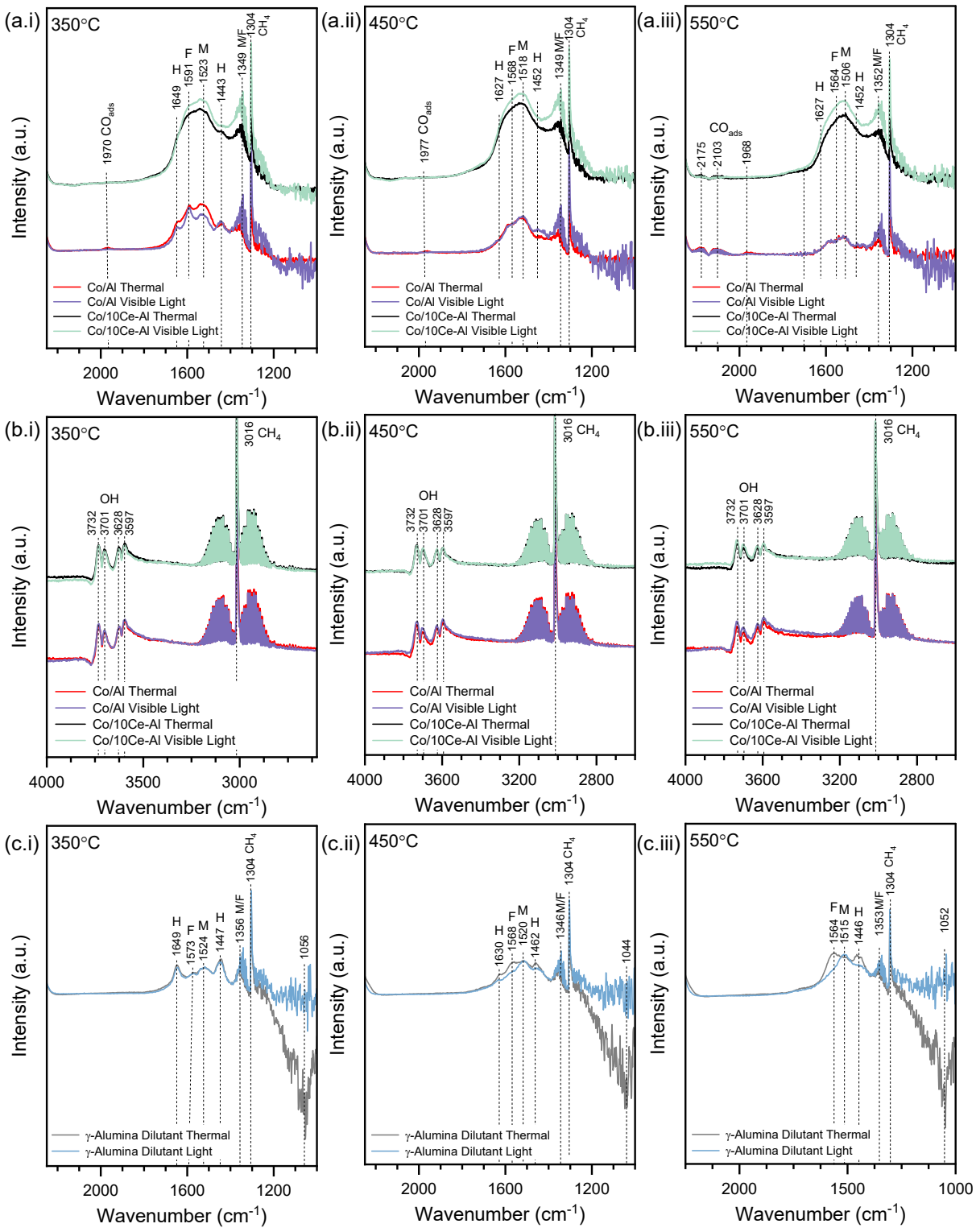

Figure S23: In-situ *DRIFTS of Co/Al (red = thermal, purple = visible light), Co/10Ce-Al (black = thermal, green = visible light) in the (a) C–O fingerprint region, (b) O–H/C–H fingerprint region and (c) C–O fingerprint region of the commercial γ-Al_2O_3 dilutant (grey = thermal, blue = visible light) at (i) 350 °C, (ii) 450 °C and (iii) 550 °C. Both catalysts were reduced and passivated* ex-situ *at 850 °C for 1 h, followed by* in-situ *re-reduction at 550 °C for 1 h. GHSV = 12 000 h^{-1}, CH_4/CO_2 = 1. All spectra are normalised to the integrated area corresponding to gaseous CO_2 (2200 – 2400 cm^{-1}) of the Co/Al catalyst at 350 °C under thermal reaction conditions.*

Besides an intensity increase, the surface adsorbed species in the C-O fingerprint region for Co/10Ce-Al (black line, Figure S23a) were akin to the Co/Al catalyst under thermal conditions. Like Co/Al, HCO_3^- and formate were evident at 350 °C before the reaction and reduced significantly in intensity by 550 °C, signifying no change in the active species with Ce incorporation. Monodentate carbonate was also an inactive species at this temperature. Before the reaction commenced, a broad CO_{ads} peak was observed, corresponding to linearly adsorbed CO. This peak decreased by 450 °C before disappearing before 550 °C, indicating that the species was active. The v(CO) mode of adsorbed CO was scarcely evident at 350 and 450 °C. CO_{ads} disappeared entirely by 550 °C, inferring that the removal of CO is rapid and therefore unmeasurable for these equilibria spectra.

Upon illumination with visible light ($400 < \lambda < 780$ nm, $I_v = 40$ mWcm^{-2}), there was no significant change in the Co/Al spectra (purple line, Figure S23a) bar a marginal decrease in the amount of hydrogen carbonate at 450 °C. On the contrary, Co/10Ce-Al (green line, Figure S23a) exhibited an increase in the formate and monodentate carbonate species and no change to HCO_3^- at 350 °C. *In-situ* DRIFTS of the similar Sabatier reaction demonstrated the same impact in the presence of CeO_2, whereby the visible light illumination facilitated the stabilisation of the formate intermediate through enhanced H_2 disassociation [14,24]. Furthermore, at 350 °C, the CO_{ads} vibrational mode at 1970 cm^{-1} was no longer evident for either catalyst, indicating that the light promotes its release. Once the reaction commenced by 550 °C, illumination with visible light prompted a negligible decrease in the surface adsorbed material (beyond thermal effects). Figure S23a and b show comparable thermal and visible light-assisted activity. The small improvement in activity under light for Ce-incorporated materials was only evident at 600 °C when sufficient energy was provided to catalyse the reaction. The lack of changes in both C–O and O–H/C–H regions upon illumination indicates that the light had no significant impact on the reaction mechanism.

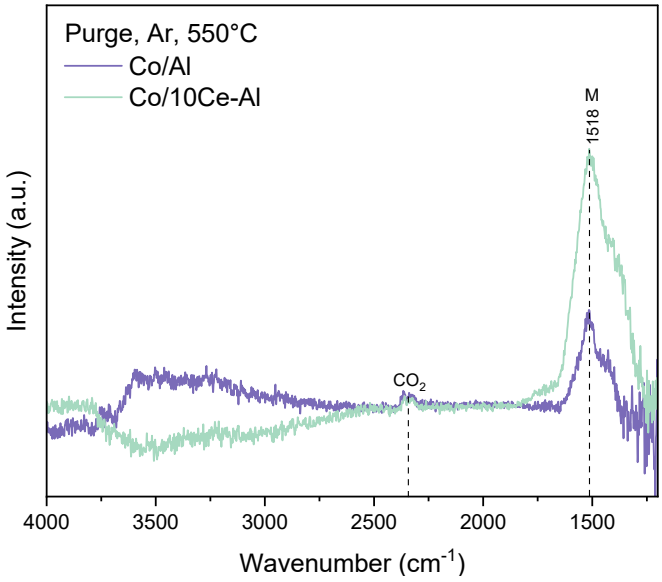

Figure S24: Residual species after purging the Co/Al and Co/10Ce-Al surface with Ar (24 mLmin^{-1}) for 1 h at 550 °C, after the in-situ *DRIFTS of the reaction (both taken under visible light conditions). The purpose of the purge was to remove any weakly absorbed and inactive material from the surface. Monodentate carbonate 'M' and residual CO_2 were all that remained.*

The catalysts were diluted in a 1/1 ratio with commercial γ-Al_2O_3 to limit carbon build-up and prevent reactor blockages. *In-situ* DRIFTS was performed on the dilutant to identify its contribution to surface-adsorbed species. Under thermal conditions (grey line, Figure S23c), there was a small concentration of monodentate carbonate, hydrogen carbonate, and formate species in positions comparable to the Co/Al catalyst. Relative to the other species, the hydrogen carbonate exhibited a stronger intensity at 350 °C, which decreased with temperature. Conversely, the monodentate carbonate peak increased with temperature, suggesting that the hydrogen carbonate decomposed to form monodentate carbonate. A significant negative peak was evident at ~ 1050 cm^{-1}, which is attributed to the dehydroxylation of Al_2O_3 [25]. This peak was not evident upon illumination (blue, Figure S23c), indicating that light prevented the dilutant dehydroxylation. At 350 °C, there were no changes under light, but the concentrations of formate and hydrogen carbonate decreased, and the monodentate carbonate species increased, indicating that light likely promoted the formation of monodentate carbonate species.

S16 References

1 Z. Liu, J. Li, M. Buettner, R. V Ranganathan, M. Uddi and R. Wang, *ACS Appl Mater Interfaces*, 2019, **11**, 17035–17049.

2 L. Mädler, H. K. Kammler, R. Mueller and S. E. Pratsinis, *J Aerosol Sci*, 2002, **33**, 369–389.

3 R. A. Young and D. B. Wiles, *Advances in X-ray Analysis*, 1980, **24**, 1–23.

4 S. Loridant, *Catal Today*, 2021, **373**, 98–111.

5 A. A. Esmailpour, S. Moradi, J. Yun, J. Scott and R. Amal, *Catal Sci Technol*, 2019, **9**, 5979–5990.

6 Q. Zhang, M. Mao, Y. Li, Y. Yang, H. Huang, Z. Jiang, Q. Hu, S. Wu and X. Zhao, *Appl Catal B*, 2018, **239**, 555–564.

7 A. Choya, B. de Rivas, J. R. González-Velasco, J. I. Gutiérrez-Ortiz and R. López-Fonseca, *Appl Catal A Gen*, 2020, **591**, 117381.

8 K. Kneipp, *Phys Today*, 2007, **60**, 40–46.

9 T. Das and G. Deo, *J Mol Catal A Chem*, 2011, **350**, 75–82.

10 L. Falbo, C. G. Visconti, L. Lietti and J. Szanyi, *Appl Catal B*, 2019, **256**, 117791.

11 X. Wang, M. Shen, L. Song, Y. Su and J. Wang, *Physical Chemistry Chemical Physics*, 2011, **13**, 15589–15596.

12 L. Ji, J. Lin and H. C. Zeng, *J Phys Chem B*, 2000, **104**, 1783–1790.

13 T. H. Nguyen, H. B. Kim and E. D. Park, *Catalysts*, 2022, **12**, 212.

14 G. E. P. O'Connell, T. H. Tan, J. A. Yuwono, Y. Wang, A. Kheradmand, Y. Jiang, P. V Kumar, R. Amal, J. Scott and E. C. Lovell, *Appl Catal B*, 2024, **343**, 123507.

15 A. Cárdenas-Arenas, A. Quindimil, A. Davó-Quiñonero, E. Bailón-García, D. Lozano-Castello, U. De-La-Torre, B. Pereda-Ayo, J. A. González-Marcos, J. R. González-Velasco and A. Bueno-López, *Appl Catal B*, 2020, **265**, 118538.

16 C. Binet, M. Daturi and J.-C. Lavalley, *Catal Today*, 1999, **50**, 207–225.

17 K. Deng, L. Lin, N. Rui, D. Vovchok, F. Zhang, S. Zhang, S. D. Senanayake, T. Kim and J. A. Rodriguez, *Catal Sci Technol*, 2020, **10**, 6468–6482.

18 Z. Sheng, H.-H. Kim, S. Yao and T. Nozaki, *Physical Chemistry Chemical Physics*, 2020, **22**, 19349–19358.

19 V. Lochař, *Appl Catal A Gen*, 2006, **309**, 33–36.

20 P. K. Huttunen, D. Labadini, S. S. Hafiz, S. Gokalp, E. P. Wolff, S. M. Martell and M. Foster, *Appl Surf Sci*, 2021, **554**, 149518.

21 Z. Lv, S. Zhu, S. Wang, M. Dong, Z. Qin, J. Wang and W. Fan, *Appl Catal A Gen*, 2023, **665**, 119378.

22 K. Lorber, J. Zavašnik, J. Sancho-Parramon, M. Bubaš, M. Mazaj and P. Djinović, *Appl Catal B*, 2022, **301**, 120745.

23 Z. Rao, K. Wang, Y. Cao, Y. Feng, Z. Huang, Y. Chen, S. Wei, L. Liu, Z. Gong, Y. Cui, L. Li, X. Tu, D. Ma and Y. Zhou, *J Am Chem Soc*, 2023, **145**, 24625–24635.

24 T. H. Tan, B. Xie, Y. H. Ng, S. F. B. Abdullah, H. Y. M. Tang, N. Bedford, R. A. Taylor, K.-F. Aguey-Zinsou, R. Amal and J. Scott, *Nat Catal*, 2020, **3**, 1034–1043.

25 X. Liu, *The Journal of Physical Chemistry C*, 2008, **112**, 5066–5073.